



Design and analysis of high-sensitivity tunable graphene sensors for cancer detection

Bahareh Amini¹ · Zahra Atlasbaf¹

Received: 22 December 2022 / Accepted: 12 February 2023 / Published online: 25 March 2023
© The Author(s), under exclusive licence to Springer Science+Business Media, LLC, part of Springer Nature 2023

Abstract

A new metamaterial refractive index sensor based on the impedance matching idea is suggested to provide an ultra-narrowband absorption response at terahertz frequencies. In order to accomplish this, the graphene layer has been modeled as circuit components using the recently developed transmission line method and the recently proposed circuit model of Periodic Arrays of Graphene Disks. The given research gives a flowchart and equations for designing a sensor, greatly simplifying the sensor design approach. This study only explores Periodic Arrays of Graphene Disks but we think the offered technique is extensible to any available graphene forms that past designers supplied with a circuit model. We compare and contrast the full-wave simulation results with the suggested circuit model. The metallic ground prohibited the transmission of the episode wave, and all occurrence electromagnetic waves are restricted in the basic design between the graphene disk. As a consequence, a perfect narrowband absorption peak is obtained. Disk absorption spectra have been discovered for a variety of refractive lists. The findings of the circuit model and full-wave simulations appear to be balanced. This RI sensor is suitable for biomedical sensing because of the combination of its features. The proposed sensor's performance as a cancer early detection sensor was evaluated among biomedical sensors, and the findings indicated that the proposed sensor is an excellent candidate for this application.

Keywords Analyte · Refractive index sensor · Graphene · Metasurface · Circuit model · Transmission line method · Cancer · Biomedical sensing

1 Introduction

The uncontrolled and abnormal growth of cells in various parts of the body is what leads to cancer. These cells may occasionally expand into other tissues beyond their natural boundaries. This is known as metastasis, a significant reason for disease mortality. According to the World Health Organization, cancer is the second leading cause of death worldwide. Due to systemic immunodeficiency, cancer patients are more susceptible to Covid-19 infection than other groups. Scientific studies indicate that approximately 4% of Covid-19

✉ Bahareh Amini
baharehamini@modares.ac.ir

¹ Faculty of Electrical Engineering, Tarbiat Modares University, Tehran, Iran

patients have some form of cancer, which either causes severe Covid19 symptoms or results in patient mortality. Early detection and treatment can reduce cancer mortality. Lung, colorectum, liver, stomach, and breast cancer were predicted to kill 1.796, 0.935, 0.83, and 0.768 million people in 2020 (Cao et al. 2021; Rastgordani and Kashani 2020a). The problems and forms of cancer therapy are determined by the stage of the disease. A wide range of cancer detection technologies, including radioimmunoassay, magnetic resonance imaging, sonography, and others, have been developed over time to satisfy a variety of criteria. Magnetic resonance and computed tomography are often used to identify cancer cells *in vivo* and *in vitro*, although certain contrast agents restrict their resolutions (Sung et al. 2021). Near-infrared fluorescence imaging is useful for identifying cancerous cells or tissues due to its low background scattering and high penetration into the tissue. However, the image and dye's shortcomings, such as limited photostability, low detection sensitivity, and low spatial resolution, render it unsuitable for *in vivo* cancer imaging. Furthermore, time-resolved fluorescence assays, gas chromatography-coupled mass spectroscopy, electrochemiluminescent immunoassays, and others are being employed for the first screening of cancer patients in centralized and hospital-based labs (Liao et al. 2021). Even though these methods have improved in terms of specificity and sensitivity, they still have a number of disadvantages, such as being time-consuming, expensive, requiring expensive and sophisticated equipment, necessitating a time-consuming pretreatment and analysis process, and not being able to detect cancer in its earliest stages (Borowczyk et al. 2021). Therefore, it is essential for cancer prevention and disease management to develop safer and more effective methods for cancer detection and treatment (Ferlay et al. 2021), particularly for cancer diagnosis. The study of liquid sensing is crucial because liquid analytes are frequently used in the biological and industrial sectors (Kayal et al. 2020; Ma et al. 2020). Terahertz (THz) modulated sensors are regarded as nondestructive inspection instruments because of their unique qualities of low photon energy and great penetration (Rastgordani et al. 2019a). These sensors may directly estimate the refractive index of analytes by non-contact monitoring of changes in the absorption spectrum (Sotsky et al. 2021). Microfluidic chips are commonly used to improve detection capabilities by sensing and detecting small amounts of liquid analyte. The poor response of natural materials to THz waves, on the other hand, restricts the precision and stability of THz sensors. THz sensors' sensitivity and accuracy for liquid analytes with equivalent refractive indexes would almost probably be limited as a result.

Terahertz technology has drawn substantial interest from the engineering community in recent decades due to its unique position in a variety of important applications such as sensing, biosensing, imaging, indoor communications, medicinal, and security applications (Ma et al. 2020; Rastgordani et al. 2019a; Sotsky et al. 2021). THz spectrum has advantages such as higher operating frequency, dimension reduction, low photon energy, and nonionizing features (Failed 2022). Furthermore, due to the rapid advancement of nanotechnology in a variety of scientific and industrial fields, as well as the use of novel materials such as graphene, the Terahertz spectrum (roughly from 100 GHz to 10 THz) has emerged as a promising region for the realization of high-quality and high-efficiency modern plasmonic devices (Ma et al. 2020; Tang et al. 2016). A metamaterial (MTM) is a substance that is designed to be built from natural materials but does not exist in nature. Metamaterials can have a negative refractive index, inverse Doppler effects, super-lenses, artificial magnetism, and invisibility cloaking (Yeo et al. 2011; Amini and Atlasbaf 2022; Chaharmahali et al. 2020). When the refractive index is negative, the electric permittivity (ϵ) and magnetic permeability (μ) are both negative, resulting in a negative reflection. High-sensitivity THz sensors based on metamaterial absorbers have received a lot of

interest in recent years (Rastgordani et al. 2021; Faruk and Sabah 2019). The resonant peak frequency is sensitive to the refractive index of the test medium (analyte), allowing for the development of a highly sensitive THz sensor. For terahertz researchers, graphene is one of the most intriguing metamaterials. Graphene is a two-dimensional (2D) single-layer structure composed of carbon atoms arranged in a honeycomb pattern. When compared to other plasmonic metals such as gold and silver, graphene offers surface plasmonic polaritons (SPPs) with strong electric field limitations and low-loss optical features in the far infrared to THz band (Rastgordani et al. 2021; Abdulkarim et al. 2022). Due to the substantial amount of modal confinement in graphene-insulator surfaces, graphene plasmonic sensors can also improve detecting characteristics (Failed 2022). In comparison to traditional materials, we may modify its surface conductivity by applying an external DC-bias voltage. The control of graphene conductivity is caused by a change in the Fermi level, which may be utilized to modify the resonance peak frequency of an absorber across a large range (Asgari and Fabritius 2021). Two THz refractive index sensors with a periodic array of graphene disks on dielectric material and gold metallic ground on the opposite side are presented in this study. The incoming terahertz waves are reflected by a gold mirror, which has adjustable absorption in reflection mode and minimal transmission. The design technique is based on the Fabry Perot resonator idea, which achieves the appropriate sensitivity in the structure's specific operating frequency by using a mathematical term. All of the techniques in this study may be performed analytically without the need for an optimization algorithm to optimize the dimensions.

2 Structure of the sensor I and the equivalent transmission line model

The finite integration method of the CST microwave studio 2019 software was used to simulate the suggested metamaterial (MTM) sensor. Using this program, many numerical calculations can be used to describe MTMs. The unit cell of the proposed structure is shown in Fig. 1. The plane wave is incident along the z-axis, and the x- and y-axes have periodic boundary conditions. The impedance match between the resonator and free space can be achieved by adjusting the design parameters. This increases incident wave absorption and reduces wave reflection, as shown in Fig. 1c. A single layer of

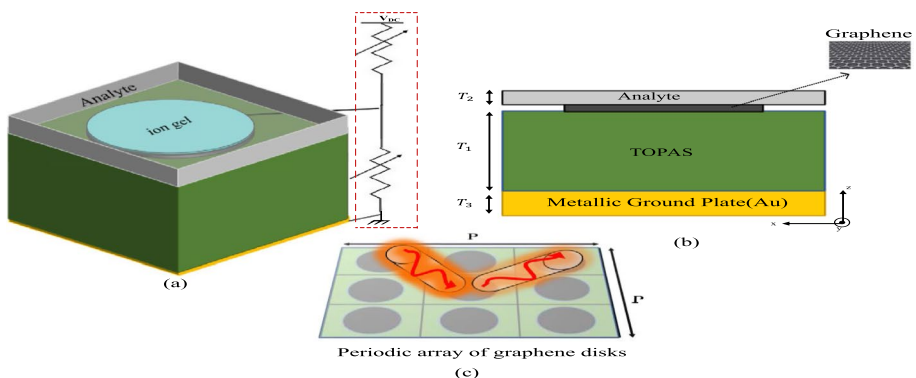


Fig. 1 The schematic view of the proposed graphene-based sensor composed of PGDM **a** perspective view. **b** side view. **c** top view

periodic graphene disk arrays, a layer of a dielectric substrate, and a layer of a metallic reflector, typically made of gold, comprise the sensor structure (Biabanifard et al. 2020; Aidinis et al. 2021). According to circuit modeling (Khatami et al. 2022), the conductivity of the gold reflector is estimated to be ($\sigma = 4.56 \times 10^7$), making it a short-circuit even in the THz region. It is important to note that the Au reflector is thick enough to prevent terahertz waves from entering. Consequently, the Au reflector's thickness has been set at 1 μm . The determination of a substrate is significant in light of the fact that the creation cycle and life expectancy of the gadget are reliant upon picking the right material for the substrate. The low losses at the THz frequency range of the polyethylene cyclic olefin copolymer (TOPAS COC with $n_d = 1.5$) have been chosen for this work. The dielectric properties of TOPAS COC material make it ideal for THz applications. The thicknesses of the TOPAS COC (T_1), the disk graphene, and the sensing medium (T_2) are, respectively, 25 and 1 μm , and the single-disk graphene P has a period of 13.84 μm .

The Kubo formula's graphene conductivity describes its properties. This formula indicates graphene's conductivity over a wide frequency range, including terahertz, σ_g can be written as follows in the following relation (Rastgordani et al. 2020):

$$\sigma_g(\omega, \mu_c, \tau, T) = \sigma_{\text{intra}}(\omega, \mu_c, \tau, T) + \sigma_{\text{inter}}(\omega, \mu_c, \tau, T) \tag{1}$$

$$\sigma_{\text{intra}}(\omega, \mu_c, \tau, T) = \frac{2k_B e^2 T}{\pi \hbar^2} \ln \left[2 \cosh \left(\frac{\mu_c}{2k_B T} \right) \right] \frac{i}{\omega + i\tau^{-1}} \tag{2}$$

$$\sigma_{\text{inter}}(\omega, \mu_c, \tau, T) = \frac{e^2}{4\hbar} \left[H\left(\frac{\omega}{2}\right) + \frac{4i\omega}{\pi} \int_0^\infty \frac{H(\epsilon) - H\left(\frac{\omega}{2}\right)}{\omega^2 - 4\epsilon^2} d\epsilon \right] \tag{3}$$

where:

$$H(\omega) = \sinh [\hbar\epsilon/k_B T] / \left\{ \cosh \left[\frac{\mu_c}{k_B T} \right] + \cosh [\hbar\epsilon/k_B T] \right\} \tag{4}$$

ω is Radian angular frequency, μ_c is Fermi energy level, τ is Relaxation time, T is Absolute temperature, K_B is Boltzmann's constant, e is Electron charge, \hbar is reduced Planck's constant.

The graphene layer's extremely thin thickness is indicated by $\mu_c = 0.08 \text{ eV}$, $\Delta = 1 \text{ nm}$, and $T = 300^\circ\text{K}$, which is the standard for ambient temperature in this study. In the terahertz frequency range, the Pauli Exclusion principle states that when $\mu_c \gg k_B T$, the inter-band conductivity is negligible. As a result, the simplified conductivity relation between graphene and a Drude-like model is as follows:

$$\sigma(\omega, \mu_c, \tau, T) = \frac{e^2 \mu_c}{\pi \hbar^2} \frac{i}{\omega + i\tau^{-1}} \tag{5}$$

The transmission line method is used to generate the metasurface sensor's equivalent circuit model. A series RLC branch model for a layer of graphene disk with a periodic configuration has been proposed for the circuit model of a single-disk graphene metasurface sensor, and it is depicted in Fig. 2, the impedance of the RLC branches of the model series (Biabanifard and

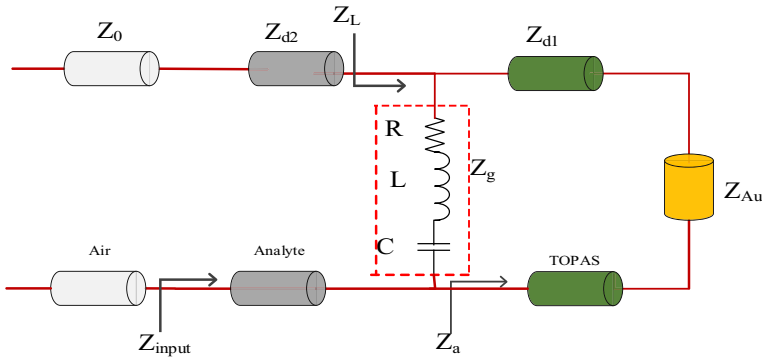


Fig. 2 The developed circuit model of the proposed sensor

Abrishamian 2018). The following formula can be used to determine the proposed absorber’s TLM input impedance for the normal THz incident wave:

$$Z_a = jZ_{d1} \tan(\beta_{d1} T_1), Z_{Au} \cong 0 \tag{6}$$

$$Z_L = Z_a \parallel Z_g \tag{7}$$

$$Z_{input} = Z_{d2} + \frac{Z_L + jZ_{d2} \tan \beta_{d2} T_2}{Z_{d2} + jZ_L \tan \beta_{d2} T_2} \tag{8}$$

where the impedance of free space is $Z_0 = 120\pi$ and that of the ground is $Z_{Au} = 0$ due to the fact that the gold layer’s thickness is greater than the terahertz wave’s penetration depth. Additionally, the substrate’s impedances, $Z_{d1} = Z_0/n_{d1}$, and $Z_{d2} = Z_0/n_{d2}$ respectively, are added, and the substrate layers’ wave propagation constants are $\beta_{d1} = 2\pi f n_{d1}/c$ and $\beta_{d2} = 2\pi f n_{d2}/c$, where f denotes the work frequency range and c denotes the speed of light. As a result, the following formula is used to determine the proposed circuit model’s reflection coefficient:

$$\Gamma = \frac{Z_{input} - Z_0}{Z_{input} + Z_0} \tag{9}$$

When the incident wave is perpendicular to the surface, the formula yields the absorption A from the S-parameters.

$$A = 1 - |S_{21}(\omega)|^2 - |S_{11}(\omega)|^2 \tag{10}$$

S_{11} and S_{21} are the reflection and transmission coefficients, respectively. With the transmission coefficient equal to zero, $|S_{21}(\omega)|^2 = 0$ there is little transmission across the structure. As a result, the simplified form for calculating absorption for the suggested device is used.

$$A = 1 - |S_{11}(\omega)|^2 = 1 - |\Gamma|^2 \tag{11}$$

The inductance, capacitance and resistance of the graphene disk can be calculated using circuit theory as follows (Barzegar-Parizi et al. 2015):

$$Z_g = R_g + j\omega L_g + \frac{1}{j\omega C_g} \tag{12}$$

$$R_g = \frac{k_n P^2 \hbar^2}{\pi S_n^2 e^2 \mu_c \tau} \tag{13}$$

$$L_g = \frac{k_n P^2 \hbar^2}{\pi S_n^2 e^2 \mu_c} \tag{14}$$

$$C_g = \frac{S_n^2 P^2 \epsilon_{eff}}{k_n P^2 q_{11}} \tag{15}$$

In which ϵ_{eff} , \hbar , and e are the average permittivity of the medium, the reduction Planck’s constant and the electron charge respectively. In detail, $\epsilon_{eff} = \epsilon_0(1 + \epsilon_d)/2$, ϵ_0 is the dielectric permittivity of the air and $\epsilon_d = n_d^2$ is the relative permittivity of the dielectric material. In Table 1, The first eigenvalue for the disk’s surface current equation is q_{11} . In this research, the parameters of the first mode of the resonance frequency of a single-disk graphene metasurface sensor are $S_1 = 0.6087r$, $K_1 = 1.2937$ (Chen et al. 2021). Equation (16) is then used to get the fill factor of the graphene array disk, $2a/P$ (Daraei et al. 2020).

$$\frac{2a}{P} = \sqrt{\frac{k_1 \hbar^2}{0.093\pi \mu_c \tau R_g e^2}} \tag{16}$$

$$a = \frac{r_1 e^2 \mu_c}{\pi \omega_0^2 \hbar^2 \epsilon_{eff}} \tag{17}$$

$$r = a \times q_{11} \tag{18}$$

where the disk’s radius is a and $a = 2.42 \mu m$. $L_g = \tau R_g$ according to Eq. (14). The inductive value is computed using the assumptions $R_g = Z_0$ and $\tau = 3$ ps. Thus, the capacitance value is obtained by using $C_g L_g = 1/\omega_0^2$, the resonance condition of the RLC circuit. Furthermore, the patterned graphene disks’ period cannot exceed their diameter, so $2a/P$ must be less than unity. The technique for designing such that the quantity of capacitor, inductor, and resistor components pulled within the feasible ranges for an absorber in the THz spectrum is discussed below. The quantity of the fill factor, $2a/P$, is chosen at the start as an arbitrary value. A high fill factor causes the PAGDs to have a higher quantity of capacitive elements; conversely, a lower fill factor causes the PAGDs to have a smaller number of

Table 1 Eigenvalues of the equation governing the surface current on graphene disks

2r/P	0.1	0.5	0.9
rq11	0.539	0.527	0.417

capacitive elements. Because a narrowband absorption response requires less capacitance than a broadband absorption response, $2a/p < 0.35$ is a reasonable and appropriate assumption that should be used. When this consideration is combined with Eq. (12) to Eq. (15), the period of the PAGDs is computed as follows:

$$P = \sqrt{\frac{S_1^2 \pi^2 \epsilon_{eff}}{k_1 C_g q_{11}}} \tag{19}$$

Then, the relation $a = P \times FF/2$, where FF is the value of the fill factor, could be used to determine the disks' radius. In addition, with regard to Eq. (14), the following factors determine graphene's chemical value (Rastgordani and Kashani 2020b):

$$\mu_c = \frac{k_1 P^2 \hbar^2}{\pi S_1^2 e^3 L_g} \tag{20}$$

In Fig. 3. the complete design flow of the analytical method.

3 Simulation results and discussion of the Sensor I

The proposed metasurface's characteristics of reflection (R), transmission (T), and absorption (A) are depicted in Fig. 4a at the normal incidence angle. These characteristics include a band of perfect absorption peaking at 99.9%, negligible transmission, and highly efficient reflection within a frequency range of 1.4–2.2 THz. Because the conductivity qualities of graphene may be modified in various ways, such as chemical doping or electrical gating, the absorber's absorption rate can be optimized. Figure 4 depicts the absorption spectra of the suggested structure for certain graphene parameters such as $\tau = 3$ ps, $\mu_c = 0.08$ eV, and $T = 300^\circ\text{k}$. The capacity to alter the position of the resonance peak for a sensor with a central frequency of 1.8 THz is demonstrated in Fig. 4b. As illustrated in Fig. 4b, changing the chemical potential value from $\mu_c = 0.08$ – 0.38 eV shifts the location of the resonance peak from $f_0 = 1.8$ to 3.5 THz.

Figure 5a depicts the normalized input impedance of the suggested structure with a central frequency of 1.8 THz in two districts real and imaginary. At $f_0 = 1.8$ THz, the structural impedance is matched to free space. The structure's analytical circuit model is executed using an easy-to-implement MATLAB algorithm. Following that, the EM response of the planned structure was evaluated using FEM, which was obtained using the CST Microwave Studio Full-wave simulation software and the frequency-domain electromagnetic solver.

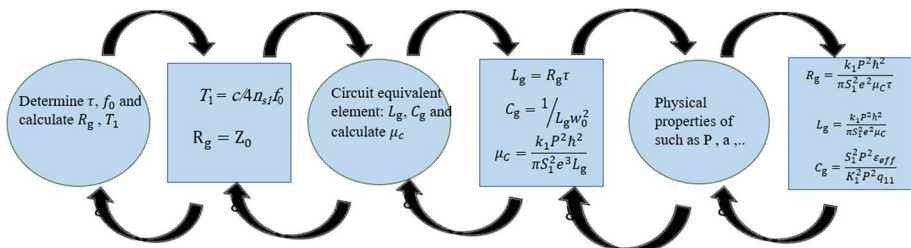


Fig. 3 The complete design flow of the analytical method

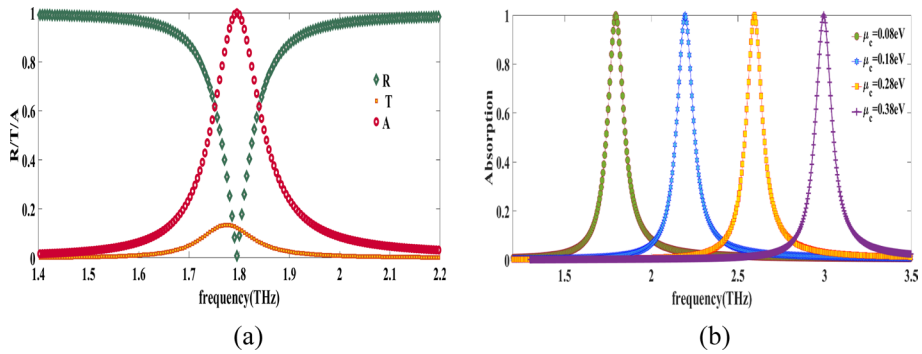


Fig. 4 **a** The reflection (R), transmission (T), and absorption (A) characteristics of the proposed metasurface at a normal incidence angle **b** The tunability of the resonance peak with chemical potential variations for sensor with central frequency of 1.8

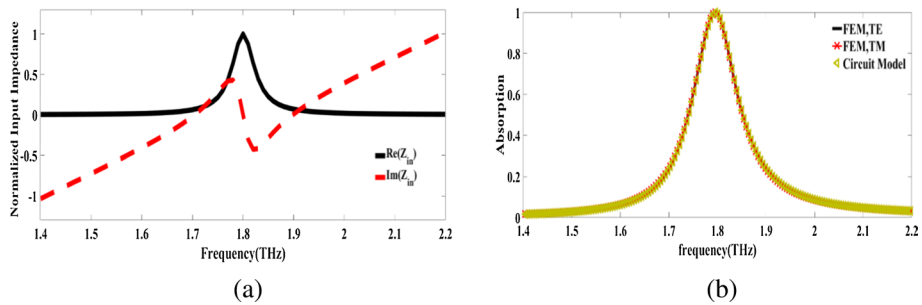


Fig. 5 **a** The Normalized input impedance and absorption spectra of the designed sensor **b** Spectra of the absorption achieved by applying the equivalent circuit model and the FEM for TE and TM modes

These two distinct approaches are used to investigate the device’s absorption spectra, as depicted in Fig. 5b so that Full-wave numerical modeling simulations using both TE and TM polarized plane waves at normal incidence illuminate the structure. By precise analysis of Fig. 5b, it can be concluded that the circuit model approach and Full-wave numerical modeling are verifying each other and that the structure response to TE and TM polarized waves is the same.

Sensing is one of the numerous uses of perfect MTM absorbers that has recently gained a lot of interest from academics and scientists. In this part, we look at the sensor’s specifications as well as its performance. The sensor is made up of an absorber and a layer of test media (analyte) on top of a graphene disk. The thickness of the analyte is 1 μm. The substance to be examined is the analyte layer. Depicts the metasurface sensor’s full-wave simulation results for various refractive indices ranging from 1 to 1.5 in Fig. 6c. Raising the refractive indices shows an apparent shift in the resonance frequency. The obtained outcomes demonstrate that the metasurface sensor is highly responsive to changes in the refractive index. Also, as depicted in Fig. 6b, two breast cells, a breast normal cell (MCF10A) and a breast cancer cell (MCF7), are used as target analytes to examine the sensing performance of the proposed graphene metasurface. Analytes are not equally distributed in the sensing area in practical experiments. In this

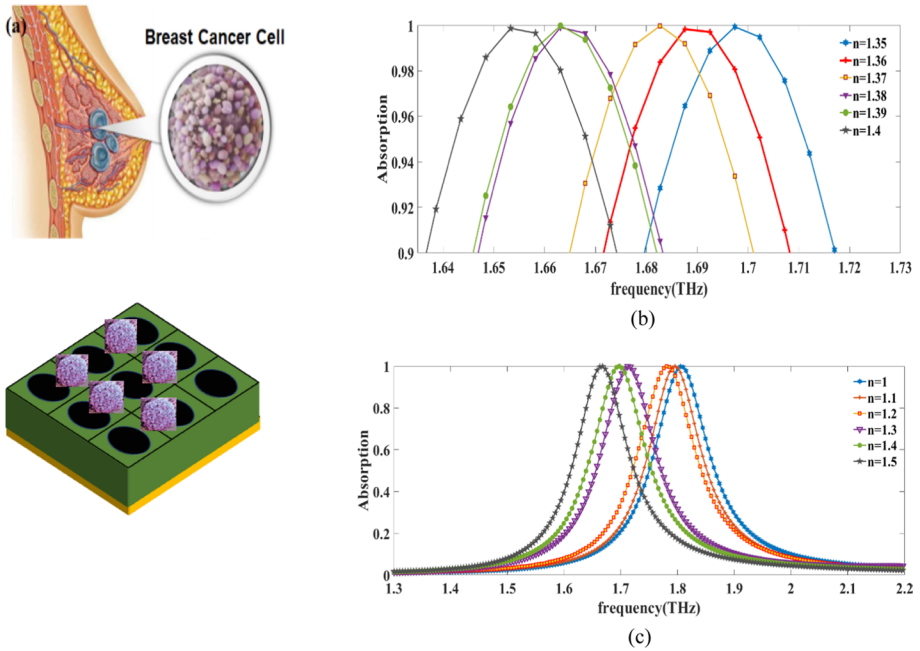


Fig. 6 a The schematic diagram of the breast cancer cell and their sensing b Absorption spectra of proposed sensor for different refractive index of MCF10A and MCF7 on the graphene metasurface c Absorption spectra of proposed sensor for different refractive index of the analyte

simulation, MCF10A and MCF7 breast cells are assumed, with comparable refractive indexes of 1.38 and 1.4. Sensitivity (S), the figure of merits (FOM), and the Q-factor are the three most essential metrics for assessing sensor performance, and they are derived using Eqs. (21–23) (Zamzam et al. 2021).

$$S = \frac{\Delta f}{\Delta n} \tag{21}$$

$$S = \frac{\Delta f}{\Delta n} \tag{22}$$

$$Q_{factor} = \frac{f}{FWHM} \tag{23}$$

Δf indicates the frequency changes of the absorption peaks, Δn represents the analyte’s RI changes, and FWHM denotes full width at half maximum in Eq. (22).

The proposed sensor’s fundamental parameters and specifications are listed in Table 3. The proposed sensor has a quality factor of 15.69, respectively. In Table 2, proposed sensor specifications are presented.

The following relation that follows can be used to calculate the absorbed electromagnetic power:

Table 2 The RPF, S, FWHM, FoM, and Q-factor using different RI of analyte for sensor

Refractive index	RPF [THz]	S [THz/RIU]	FWHM [THz]	FOM	Q-factor
1	1.80		0.113		15.92
1.1	1.79	0.1	0.107	0.93	16.72
1.2	1.78	0.1	0.117	0.85	15.21
1.3	1.71	0.7	0.113	6.19	15.13
1.4	1.69	0.2	0.107	1.86	15.79
1.5	1.66	0.3	0.108	2.77	15.37

Table 3 Comparison between the sensor specifications of reported in previous work and proposed sensor

Refs	Year	Mechanism	Operating rang [THz]	Sensitivity [THz/RIU]
Chen et al. (2013)	2013	Hybridization of magnetic and electric resonators	2–5.5	0.13
Cong and Singh (2014)	2014	Metamaterial absorber	0.4–1	0.163
Xiong et al. (2021)	2021	Metamaterial absorber	0.2–0.9	0.126
This work	2022	Metamaterial absorber	1.3–2	0.28

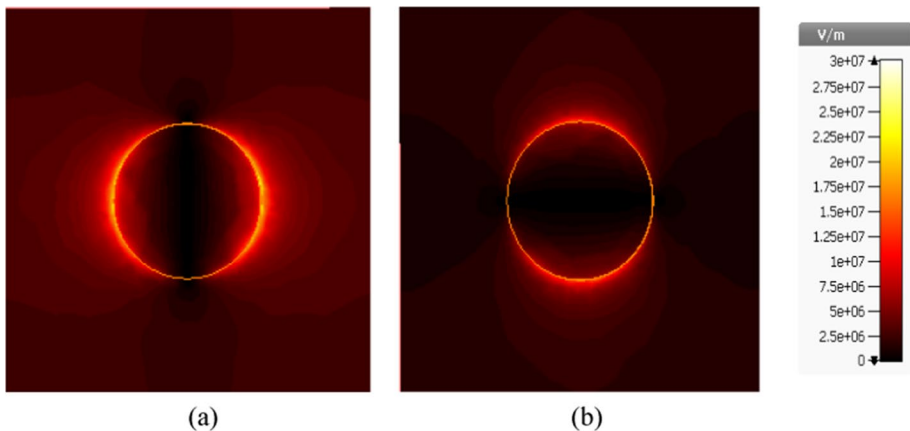


Fig. 7 Electric field distributions of the disks metasurface sensor for **a** TM mode **b** TE mode

$$P = (1/2)\omega\epsilon'' |E|^2 \tag{24}$$

where ω , ϵ'' and $|E|$ are angular frequency the material’s total electric field’s amplitude, permittivity’s imaginary part, and the material’s total electric field’s amplitude, respectively. With x-polarized light incident, the proposed metasurface sensor’s electric field distributions are depicted in Fig. 8. As depicted in Fig. 7a, b, the electric distributions for the TE and TM modes could be achieved with $n_{analyte} = 1$, and $\mu_c = 0.08$ eV, respectively.

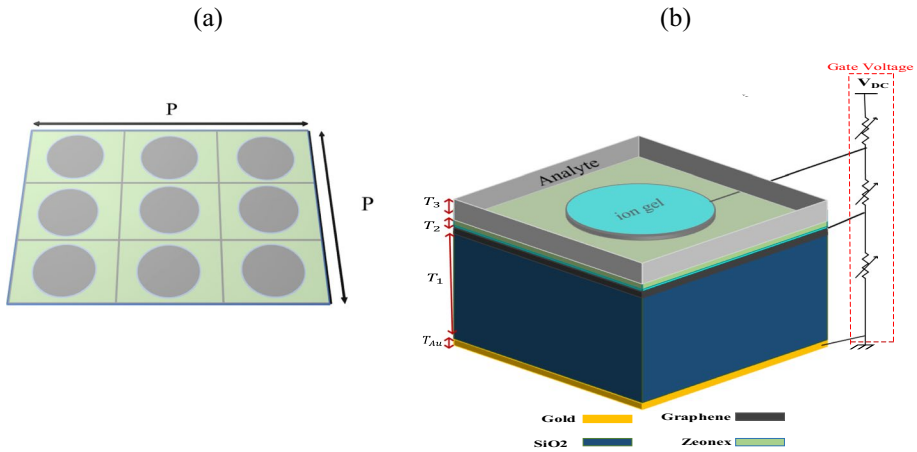


Fig. 8 The schematic view of the proposed graphene-based sensor composed of PGDM **a** top view **b** perspective view

4 Structure of the sensor II and the equivalent transmission line model

As illustrated in Fig. 8, the proposed sensor comprises periodic two-layer graphene disk arrays arranged near a metallic ground covered with dielectric spacers. Figure 8 depicts the geometrical parameters. Dielectric spacers with thicknesses of $T_1 = 18.9\mu\text{m}$, $T_2 = 5\mu\text{m}$, and $T_3 = 1\mu\text{m}$ divide the two-layer graphene disks with a diameter of $2a$. P is the disk arrays' period and is $6.3\mu\text{m}$. To facilitate the electrical gating procedure, thin graphene stripes with a thickness of 0.1 m are employed to electrically link the disk arrays (Fardoost et al. 2017). As a result, each graphene layer may be dynamically and individually modified using an external bias circuit, as illustrated in Fig. 8b. The dielectric layer is made of SiO_2 with $\epsilon_r = 3.9$. To get the best results in terahertz, we also used Zeonex, a dielectric made of cyclo-olefin polymer (COP). The relative permittivity of Zeonex is 2.34. Zeonex was chosen for its unique optical properties, including low absorption loss, high glass transition temperature, minimal material dispersion, and insensitivity to humidity, as well as its ease of injection molding or extrusion into film and sheet. It is suitable for terahertz applications because it has a very low terahertz absorption loss. Additionally, Zeonex is insensitive to the majority of solvents and acids. Consequently, it is a viable option for a terahertz absorber's substrate (Rastgardani et al. 2019b).

The following are the various sensor components' equivalent impedances (Fig. 9). We were able to achieve the total input impedance. Also, using Eq. (10), the total reflection coefficient of the proposed structure could be determined.

$$Z_a = jZ_{d1} \tan(\beta_{d1}T_1), Z_{Au} \cong 0 \tag{25}$$

$$Z_{L1} = Z_a \parallel Z_{g1} \tag{26}$$

$$Z_b = Z_{d2} + \frac{Z_{L1} + jZ_{d2} \tan \beta_{d2}T_2}{Z_{d2} + jZ_{L1} \tan \beta_{d2}T_2} \tag{27}$$

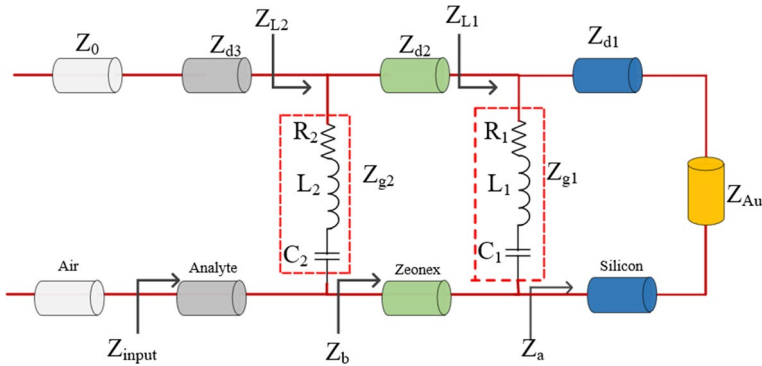


Fig. 9 The developed circuit model of the proposed sensor

$$Z_{L2} = Z_b \parallel Z_{g2} \tag{28}$$

$$Z_{input} = Z_{d3} + \frac{Z_{L2} + jZ_{d3} \tan \beta_{d3} T_3}{Z_{d3} + jZ_{L2} \tan \beta_{d3} T_3} \tag{29}$$

where the impedance of free space is $Z_0 = 120\pi$ and also, the impedance of the ground is $Z_{Au} = 0$ because the thickness of the gold layer is greater than the penetration depth of terahertz wave. Moreover $Z_{d1} = Z_0/n_{d1}$, $Z_{d2} = Z_0/n_{d2}$ and $Z_{d3} = Z_0/n_{d3}$ are the impedance of the substrates. Also, the wave propagation constants of the substrate layers are $\beta_{d1} = 2\pi f n_{d1}/c$, $\beta_{d2} = 2\pi f n_{d2}/c$ and $\beta_{d3} = 2\pi f n_{d3}/c$ which f is the work frequency range and c , is the speed of light. Where the disk's radius is $1.1 \mu\text{m}$, $\tau = 3 \text{ ps}$ and $\mu_c = 0.08 \text{ eV}$ (Fig. 10).

5 Simulation results and discussion of the Sensor II

The figure depicts the reflection (R), transmission (T), and absorption (A) properties of the proposed metasurface. Figure 10a at the normal angle of incidence. A perfect absorption band with a peak at 97%, negligible transmission, and highly efficient reflection in the 2.2–3 THz frequency range are among these characteristics. Figure 10b depicts the proposed structure's absorption curve at various chemical potentials. By shifting the graphene chemical potential from 0.08 to 0.38, the absorption amplitude decreases as well as the frequency shift of the absorption peak, as depicted in this figure. When the chemical potential of the graphene is 0.08, the absorption peak reaches its highest value.

Biomedical sensing is one of the most important uses of refractive index sensors. The typical biological analyte refractive index ranges between 1.3 and 1.5. Figure 11 depicts the simulation results for the test medium with refractive indices ranging from 1.3 to 1.4 and a step of 0.01. The suggested sensor is suitable for breast cancer sensing, as demonstrated by the simulation results and calculations.

The proposed sensor's fundamental parameters and specifications are listed in Table 4. The proposed sensor has a quality factor of 27.33, respectively. In Table 5, proposed sensor specifications are presented.

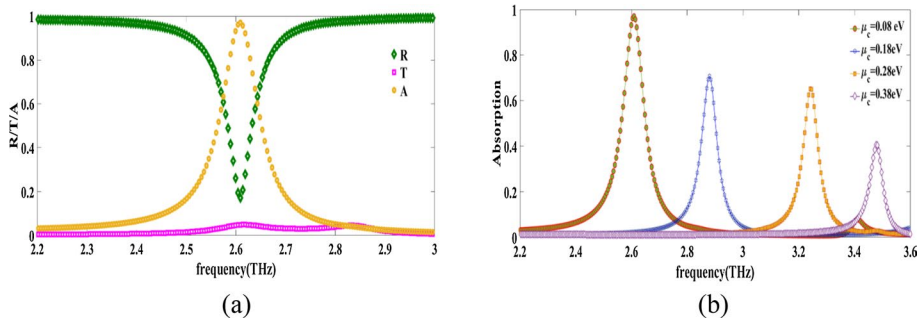


Fig. 10 **a** The reflection (R), transmission (T), and absorption (A) characteristics of the proposed metasurface at a normal incidence angle **b** The tunability of the resonance peak with chemical potential variations for sensor with central frequency of 2.6

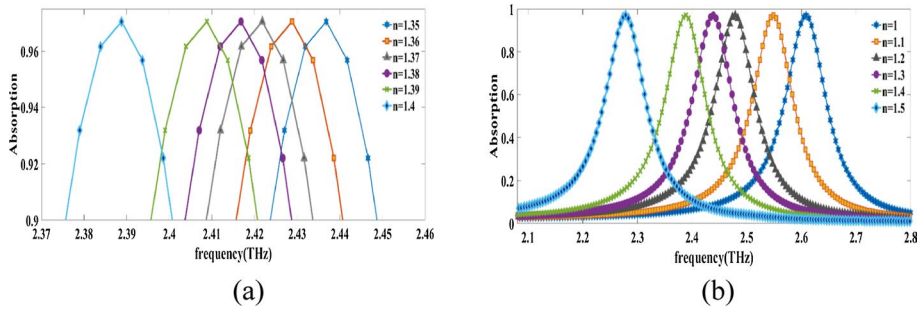


Fig. 11 **a** Absorption spectra of proposed sensor for different refractive index of MCF10A and MCF7 on the graphene metasurface **b** Absorption spectra of proposed sensor for different refractive index of the analyte

Table 4 The RPF, S, FWHM, FOM, and Q-factor using different RI of analyte for sensor

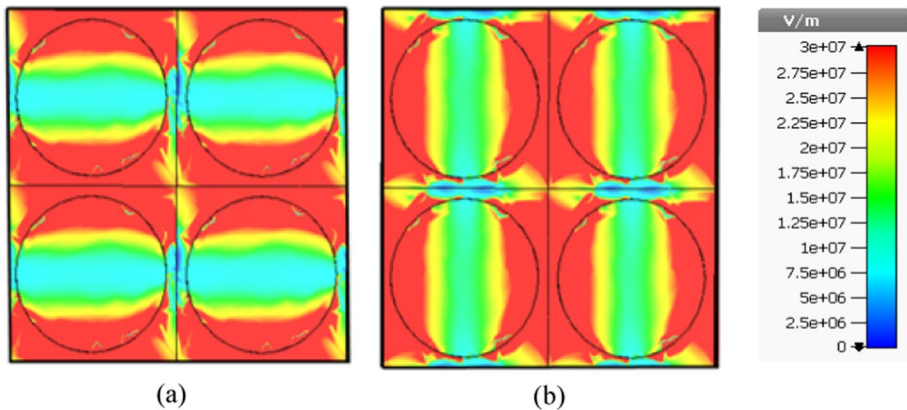
Refractive index	RPF [THz]	S [THz/RIU]	FWHM [THz]	FOM	Q-factor
1	2.6		0.09		28.88
1.1	2.54	0.6	0.089	6.74	28.5
1.2	2.47	0.7	0.091	7.69	27.14
1.3	2.43	0.4	0.09	4.44	27
1.4	2.38	0.5	0.089	5.61	26.7
1.5	2.27	1.1	0.088	12.5	25.79

The electric field distributions of the proposed metasurface absorber with the x-polarized light incident are shown in Fig. 12. As shown in Fig. 12a, b, we could achieve the electric distributions for the TE and TM modes with $\mu_c = 0.08\text{eV}$. So, the amplitude of the total electric field, $|E|$, inside the patch for the TM mode is equal to the TE mode.

Figure 13 depicts the test setup for measuring the proposed sensor’s absorption curve, and the THz pump laser generates a broad-band THz wave, which then passes through the

Table 5 Comparison between the sensor specifications of reported in previous work and proposed sensor

Refs	Year	Mechanism	Operating rang [THz]	Sensitivity [THz/RIU]
Soltani et al. (2016)	2016	Dielectric resonator	0.5–1	0.5
Tang et al. (2018)	2018	Plasmon induced transparency	1–6.5	0.36
Keshavarz and Vafapour (2019)	2019	Metamaterial reflector	1.1–2.1	0.54
Wang et al. (2020)	2020	Metasurface absorbers	0.4–2.5	0.5
Emaminejad et al. (2021)	2021	Split-ring resonator (SRR)	0.8–2.2	0.45
This work	2022	Metamaterial absorber	2.2–3	0.66

**Fig. 12** Electric field distributions of the disks metasurface sensor for **a** TE mode **b** TM mode

collimated lens and the polarizer, which may be altered as a vertical or horizontal polarised wave and is tuned based on the experimental conditions. Following that, the beam splitter divides the optical light into two equal-intensity waves. So, after passing through the lens, half of the light may be sent to the CCD camera, while the other half can be directed to the objective lens and the target device. As a result, the Optical Signal can measure the reflected wave from the target device (Norouzi Razani et al. 2022).

UV light is utilized for photolithography, whereas electron radiation is used for e-beam lithography, which implies that the photoresist is exposed to light in photolithography, whereas a focussed electron beam can be used for exposure in beam lithography. Because e-beam lithography is less expensive than photolithography, we do not need to employ a photomask in this process, whereas photolithography requires the use of a mask. Another significant distinction is that photolithography cannot be utilized for dimensions smaller than, say, $2\ \mu\text{m}$, therefore e-beam lithography can be used instead. Because of its tiny dimensions, graphene can be patterned using e-beam lithography following the transfer process, and graphene etching will be done via Reactive Ion Etching. “Fabrication process and sensing system design of the proposed sensor”, all of these steps can have fabrication errors, so, naturally, the fabricated device will have different results from the simulated case considerably. For example, the dimensions of the device after the discussed lithography techniques can be a little bit different from the simulation, or the thickness of dielectrics can be slightly different from the simulated structure. Therefore, fabrication errors

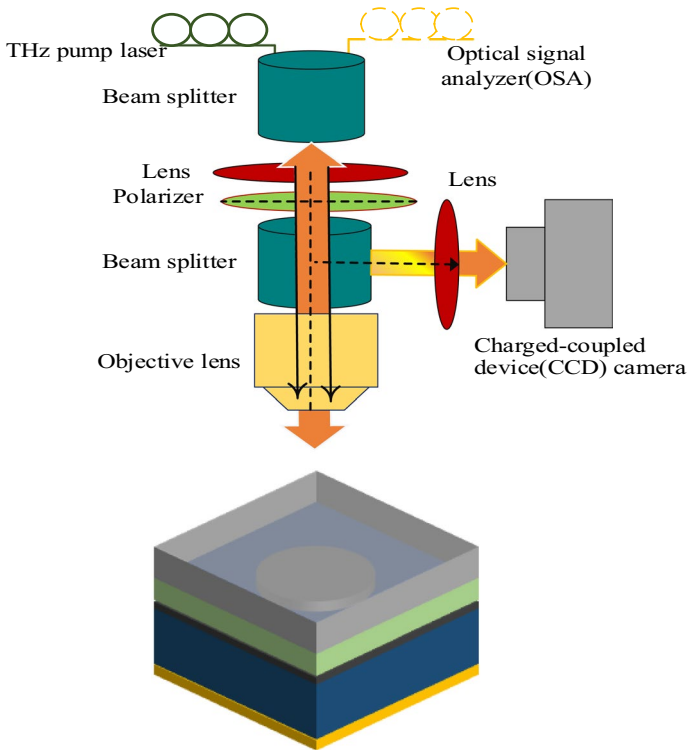


Fig. 13 The test setup for measuring the absorption curve of proposed sensor

will be expected in all of the stated procedures. Another issue is the cost of the device for fabrication, because utilizing two different lithography techniques may increase the cost of fabrication.

6 Conclusion

As a result, we investigated one-layer and two-layer graphene disk arrays and based high-sensitivity graphene metasurface refractive index sensors. We compared the results of the circuit model for various refractive records with those of the full-wave simulation for high-sensitivity sensors in order to investigate the precision of the proposed model. The proposed sensor can be used in a variety of settings, including biomedical systems. The one-layer and two-layer graphene disk arrays metasurface sensor's absorption spectra for breast cancer cells and healthy cells have prompted us to consider its potential use in biomedical systems.

Author contributions BA (Bahareh Amini) wrote the manuscript text and prepared the figures. ZA (Zahra Atlasbaf) validated the whole data and confirmed the results.

Funding No funding was received for this research.

Data availability All data generated or analyzed during this study are included in this published article.

Declarations

Conflict of interest The authors declare that they have no conflict of interest.

Consent to participate Written informed consent for participate was obtained from all participants.

Consent for publication Written informed consent for publication was obtained from all participants.

Ethical approval We declare that this article is original, has not been published before, and is not currently considered for publication elsewhere. We confirm that the manuscript has been read and approved by all named authors and that there are no other persons who satisfied the criteria for authorship but are not listed. We further confirm that the order of authors listed in the manuscript has been approved by all of us.

References

- Abdulkarim, Y.I., Awl, H.N., Muhammadsharif, F.F., Bakır, M., Alkurt, F.Ö., Altıntaş, O., Saeed, S.R., Taouzari, M., Karaaslan, M., Appasani, B., Dong, J.: A Vanadium dioxide-based metamaterial with quatrefoil and circle loaded structure on flexible polyamide substrate for terahertz applications. *Front. Phys.* **10**, 722 (2022)
- Aidinis, K., Daraei, O.M., Goudarzi, K.: Analytical design of tunable disk, patch and ribbon-patterned graphene absorbers in the terahertz spectrum. *Photonics Nanostruct. Appl.* **46**, 100951 (2021)
- Amini, B., Atlasbaf, Z.: Two new broadband and tunable terahertz pyramid patch/disk absorbers based on graphene metasurface. *Photonics Nanostruct. Fundam. Appl.* **52**, 101048 (2022)
- Asgari, S., Fabritius, T.: Graphene-based dual-functional chiral metamirror composed of complementary 90° rotated u-shaped resonator arrays and its equivalent circuit model. *Sci. Rep.* **11**(1), 23827 (2021)
- Barzegar-Parizi, S., Rejaei, B., Khavasi, A.: Analytical circuit model for periodic arrays of graphene disks. *IEEE J. Quantum Electron.* **51**(9), 1–7 (2015)
- Biabanifard, M., Abrishamian, M.S.: Multi-band circuit model of tunable thz absorber based on graphene sheet and ribbons. *AEU-Int. J. Electron. Commun.* **95**, 256–263 (2018)
- Biabanifard, M., Arsanjani, A., Abrishamian, M.S., Abbott, D.: Tunable terahertz graphene-based absorber design method based on a circuit model approach. *IEEE Access* **8**, 70343–70354 (2020)
- Borowczyk, M., Woliński, K., Więckowska, B., Jodłowska-Siewert, E., Szczepanek-Parulska, E., Verburg, F.A., Ruchała, M.: Sonographic features differentiating follicular thyroid cancer from follicular adenoma—a meta-analysis. *Cancers* **13**, 938 (2021)
- Cao, W., Chen, H.D., Yu, Y.W., Li, N., Chen, W.Q.: Changing profiles of cancer burden worldwide and in China: a secondary analysis of the global cancer statistics 2020. *Chin. Med. J.* **134**, 783–791 (2021)
- Chaharmahali, I., Soltani, M., Hoseini, M., Biabanifard, M.: Control of terahertz waves for te and tm modes using graphenebased metamaterials. *Opt. Eng.* **59**(4), 047101 (2020)
- Chen, C.Y., Yang, Y.H., Yen, T.J.: Unveiling the electromagnetic responses of fourfold symmetric metamaterials and their terahertz sensing capability. *Appl. Phys. Express* **6**(2), 022002 (2013)
- Chen, T., Jiang, W., Yin, X.: Dual-band ultrasensitive terahertz sensor based on tunable graphene metamaterial absorber. *Superlattice. Microst.* **154**, 106898 (2021)
- Cong, L., Singh, R.: Sensing with THz metamaterial absorbers, (2014), arXiv preprint [arXiv:1408.3711](https://arxiv.org/abs/1408.3711), <http://arxiv.org/abs/1408.3711v1>
- Daraei, O.M., Goudarzi, K., Bemani, M.: A tunable ultra-broadband terahertz absorber based on two layers of graphene ribbons. *Optic Laser. Technol.* **122**, 105853 (2020)
- Emaminejad, H., Mir, A., Farmani, A.: Design and simulation of a novel tunable terahertz biosensor based on metamaterials for simultaneous monitoring of blood and urine components. *Plasmonics* **16**, 1537–1548 (2021)
- Fardoost, A., Vanani, F.G., Safian, R.: Design of a multilayer graphene-based ultra wideband terahertz absorber. *IEEE Trans. Nanotechnol.* **16**, 68–74 (2017)
- Faruk, A., Sabah, C.: Absorber and sensor applications of complimentary H-shaped fishnet metamaterial for sub-terahertz frequency region. *Optik* **177**, 64–70 (2019)
- Ferlay, J., Colombet, M., Soerjomataram, I., Parkin, D.M., Piñeros, M., Znaor, A., Bray, F.: Cancer statistics for the year 2020: an overview. *Int. J. Cancer* **149**, 778–789 (2021)

- Kayal, S., Shaw, T., Mitra, D.: Design of miniaturized highly sensitive liquid sensor at microwave frequency. *Int. J. RF Microw. Comput. Aid. Eng.* **30**, e22387 (2020)
- Keshavarz, A., Vafapour, Z.: Sensing avian influenza viruses using terahertz metamaterial reflector. *IEEE Sens. J.* **19**(13), 5161–5166 (2019)
- Khatami, S.A., Rezaei, P., Zamzam, P.: Quad band metal-dielectric-metal perfect absorber to selective sensing application. *Opt. Quant. Electron.* **54**, 638 (2022)
- Liao, X., Wang, X., Li, P., Chen, S., Zhang, M., Mei, L., Qi, Y., Hong, C.: Electrochemical immunosensor using artificial enzyme-induced metallization for the ultra-sensitive detection of alpha fetoprotein. *Sens. Actuators Chem.* **344**, 130258 (2021)
- Ma, X.X., Chen, K.X., Wu, J.Y., Wang, L.F.: Low-Cost and highly sensitive liquid refractive index sensor based on polymer horizontal slot waveguide. *Photonic Sens.* **10**, 7–15 (2020)
- Norouzi Razani, A., et al.: Absorption-based ultra-sensitive RI sensor based on the flower-shaped graphene resonator for early detection of cancer. *Opt. Commun.* **524**, 128775 (2022)
- Parmar, J., Patel, S.K., Katkar, V.: Graphene-based metasurface solar absorber design with absorption prediction using machine learning. *Sci. Rep.* **12**(1), 2609 (2022)
- Rastgordani, A., Kashani, Z.G.: Robust design method for metasurface high-sensitivity sensors and absorbers. *JOSA B* **37**(7), 2006–2011 (2020a)
- Rastgordani, A., Kashani, Z.G.: High-sensitive refractive index sensors based on graphene ring metasurface. *Optic. Commun.* **474**, 126164 (2020b)
- Rastgordani, A., Kashani, Z.G., Abrishamian, M.S.: Analytical design of all-dielectric grating as a narrow-band absorber. *Opt. Commun.* **452**, 95–100 (2019a)
- Rastgordani, A., Kashani, Z.G., Abrishamian, M.S.: Generalized circuit model for all-dielectric narrowband metasurface absorbers. *Appl. Opt.* **58**(34), 9338–9344 (2019b)
- Rastgordani, A., Kashani, Z.G., Abrishamian, M.S.: A general equivalent circuit model for plasmonic metasurface broadband absorbers. *Optik Int. J. Light Electron Optic.* **221**, 165354 (2020)
- Rastgordani, A., Kashani, Z.G., Abrishamian, M.S.: Theory and algo-rithm for tunable mantle cloaking through bulk dirac semimetal metasurfaces around elliptical cylinders. *Optik* **232**, 166564 (2021)
- Soltani, A., Neshasteh, H., Mataji-Kojouri, A., Born, N., CastroCamus, E., Shahabadi, M., Koch, M.: Highly sensitive terahertz dielectric sensor for small-volume liquid samples. *Appl. Phys. Lett.* **108**(19), 191105 (2016)
- Sotsky, A.B., Nazarov, M.M., Miheev, S.S., Sotskaya, L.I.: Sensitivity of reflecting terahertz sensors of aqueous solutions. *Tech. Phys.* **66**, 305–315 (2021)
- Sung, H., Ferlay, J., Siegel, R.L., Laversanne, M., Soerjomataram, I., Jemal, A., Bray, F.: Global cancer statistics 2020: GLOBOCAN estimates of incidence and mortality worldwide for 36 cancers in 185 countries. *CA Cancer J. Clin.* **71**, 209–249 (2021)
- Tang, Q., Liang, M., Lu, Y., Wong, P.K., Wilmlink, G.J., Zhang, D., Xin, H.: Microfluidic devices for terahertz spectroscopy of live cells toward lab-on-a-chip applications. *Sensors* **16**, 476 (2016)
- Tang, P.R., Li, J., Du, L.H., Liu, Q., Peng, Q.X., Zhao, J.H., Zhu, B., Li, Z.R., Zhu, L.G.: Ultrasensitive specific terahertz sensor based on tunable plasmon induced transparency of a graphene micro-ribbon array structure. *Opt. Express* **26**(23), 30655–30666 (2018)
- Wang, Y., Zhu, D., Cui, Z., Yue, L., Zhang, X., Hou, L., Zhang, K., Hu, H.: Properties and sensing performance of all-dielectric metasurface THz absorbers. *IEEE Trans. Terahertz Sci. Technol.* **10**(6), 599–605 (2020)
- Xiong, Z., et al.: Terahertz sensor with resonance enhancement based on square split-ring resonators. *IEEE Access* **9**, 59211–59221 (2021)
- Yeo, L.Y., Chang, H.C., Chan, P.Y., Friend, J.R.: Microfluidic devices for bioapplications. *Small* **7**, 12–48 (2011)
- Zamzam, P., Rezaei, P., Khatami, S.A.: Quad-band polarization-insensitive metamaterial perfect absorber based on bilayer graphene metasurface. *Phys. E* **128**, 114621 (2021)

Publisher's Note Springer Nature remains neutral with regard to jurisdictional claims in published maps and institutional affiliations.

Springer Nature or its licensor (e.g. a society or other partner) holds exclusive rights to this article under a publishing agreement with the author(s) or other rightsholder(s); author self-archiving of the accepted manuscript version of this article is solely governed by the terms of such publishing agreement and applicable law.